Editors' Suggestion | Featured in Physics

Niobium air bridges as low-loss components for superconducting quantum hardware

N. Bruckmoser,[1,2,*] L. Koch,[1,2,†] I. Tsitsilin,[1,2] M. Grammer,[1,2] D. Bunch,[1,2] L. Richard,[1,2] J. Schirk,[1,2] F. Wallner,[1,2] J. Feigl,[1,2] C.M.F. Schneider,[1,2] S. Geprägs,[2] V.P. Bader,[2] M. Althammer,[1,2] L. Södergren,[1,2] and S. Filipp[1,2,3]

[1] *Technical University of Munich, TUM School of Natural Sciences, Department of Physics, 85748 Garching, Germany*

[2] *Walther-Meißner-Institut, Bayerische Akademie der Wissenschaften, 85748 Garching, Germany*

[3] *Munich Center for Quantum Science and Technology (MCQST), Schellingstraße 4, 80799 München, Germany*

(Received 10 June 2025; revised 19 November 2025; accepted 9 December 2025; published 3 February 2026)

Scaling up superconducting quantum processors necessitates the use of a high routing density for readout and control lines, relying on low-loss interconnects to maintain design flexibility and device performance. We propose and demonstrate a universal subtractive fabrication process for air bridges based on an aluminum hard mask and niobium as the superconducting film. Using this technology, we fabricate superconducting coplanar waveguide resonators incorporating several niobium air bridges in and across their center conductors. Through rigorous cleaning methods, we achieve mean internal quality factors in the single-photon limit exceeding $Q_{\mathrm{int}} = 8.2 \times 10^6$. Notably, the loss per air bridge remains below the detection threshold of the resonators. Due to the larger superconducting energy gap of niobium, compared with conventional aluminum air bridges, our approach enables stable performance at elevated temperatures and magnetic fields, which we experimentally confirm in temperatures up to 3.9 K and in a magnetic field of up to 1.60 T. Additionally, we utilize air bridges to realize low-loss vacuum-gap capacitors and demonstrate their successful integration in transmon qubits by achieving median qubit lifetimes of $T_1 = 51.6\ \mu\mathrm{s}$.

DOI: 10.1103/smlq-r7x6

I. INTRODUCTION

In quantum, as well as classical, microwave frequency integrated circuits, air bridges are an integral element for routing signals by leaving the substrate and thus acting as a crossover between perpendicular paths. These interconnects are necessary to enable large-scale quantum processors by increasing the density and complexity of coplanar waveguide (CPW) routing [1,2]. In addition, they play an important role in mitigating unwanted crosstalk between adjacent signal lines and parasitic modes [3–6]. Owing to their complexity, many different fabrication processes have been proposed, based on both optical [7–12] and electron beam lithography [2,13–17]. With a few exceptions [7,11,12,17,18], in most superconducting processes, aluminum (Al) is employed for air bridge metallization, with these structures typically fabricated after the Josephson junctions [2,19]. However, this sequencing imposes strict limitations: aggressive cleaning methods, such as those using hydrofluoric acid or piranha solution, cannot be used to remove surface oxides, as they would damage Al-based structures, including the junctions themselves. Additionally, post-junction processing steps must adhere to a minimal thermal budget to preserve junction integrity [20]. By instead fabricating air bridges before Josephson junctions, higher processing temperatures—during baking, sputtering, and etching—can be applied without compromising junction performance. This approach enables the use of temperature-sensitive techniques, such as laser annealing, to fine-tune qubit frequencies and mitigate frequency crowding [21,22]. Furthermore, the superconducting energy gap of niobium (Nb) is significantly higher than that of Al [23]. This leads to a higher resilience of superconductivity in the presence of magnetic fields and thus also allows for the use of galvanically connected Nb air bridges as active elements within flux lines, with typical currents of the order of 1 mA [24]. In addition, the higher superconducting critical

*Contact author: Niklas.Bruckmoser@wmi.badw.de
†Contact author: Leon.Koch@wmi.badw.de

temperature enables quantum experiments at elevated temperatures above 200 mK [25,26].

A key difficulty in using Nb for air bridges is that soft resist masks pose processing challenges. In particular, sputtered atoms penetrate underlying layers due to their high kinetic energy [27,28]. This leads to lossy interfaces on the bottom side of the air bridges, owing to the high amount of two-level systems (TLSs) that are hosted in photoresist [29]. To improve on these aspects, we develop a fabrication process based on a sacrificial hard mask that enables any complementary superconducting material, such as Nb, tantalum (Ta), or niobium-titanium nitride (NbTiN) to be used as an air bridge. Due to its low etch resistance, we use Al as a sacrificial hard mask, which easily allows us to remove the mask afterwards. With this method, we achieve substantially higher quality factors than those obtained using existing fabrication processes [8,11,18], which are comparable to standard non-air-bridge processes. These can therefore be readily used as low-loss routing elements. Moreover, our low-loss air bridge technology can also be used to form a transmon qubit by creating a capacitive shunt between the ground plane and a large overlying air bridge.

II. FABRICATION

To realize low-loss Nb sputtered air bridges, we utilize an additional thin hard mask, illustrated in Fig. 1(c), on top of the frequently used soft mask as part of the fabrication process flow. The hard mask serves three essential purposes in our fabrication process. First, it acts as a protective barrier for the bottom resist, mitigating ion implantation during argon ion milling [30]. Second, it functions as a shielding layer during sputtering, preventing intermixing between the underlying resist and high kinetic Nb particles [27,28]. Finally, the hard mask serves as a dedicated stopping layer in the reactive ion etching process [31]. This ensures precise control to prevent etching into the Nb ground plane.

Prior to the air bridge processing steps, we fabricate the groundplane of the chips containing macroscopic ($\geq$2 μm) structures, such as coplanar waveguides, ports, and qubit pads. We start with high-resistivity (>10 kΩcm) 100 mm silicon (Si) wafers that are cleaned in piranha acid (3 parts 96 wt% H_2SO_4 to 1 part 30 wt% H_2O_2) and a 7:1 buffered oxide etch (BOE) solution (7 parts 40 wt% NH_4F to 1 part 49 wt% HF) to remove lossy silicon oxides [32]. Afterwards, we immediately transfer the substrate in an ultrahigh vacuum system (PLASSYS MEB550 S4-I) to sputter-deposit a 150 nm thin film of Nb. Using maskless optical lithography, we pattern coplanar waveguide structures and transfer these into the film using an SF_6-based reactive ion etching process. After a wet-chemical resist stripping step (TechniStrip P1331), these samples act as the starting point of the hard-mask-based air bridge process [Figs. 1(a)–1(i)].

We control the bridge height of 2.7 μm by spin coating the reflow-compatible resist AZ ECI 3027 on the patterned wafer. The reflow step at 140 °C for 5 min is needed to reduce the steepness of the sidewalls and ensure the stability of released air bridges [Fig. 1(b)]. We afterwards evaporate a thin sacrificial layer of 100 nm Al as a hard mask at a wafer tilt of 20° to cover topographies in the ground plane [Fig. 1(c)]. This hard mask needs to be sufficiently thick to serve as a reproducible etch stop layer during the reactive ion etching process of the air bridges. We deposit the hard mask with electron beam evaporation instead of sputtering to reduce intermixing in the resist-aluminum interface. To create contact areas to the underlying Nb layer, we pattern a thin optical resist (AZ MiR 701) on the pads of the air bridge [Fig. 1(d)]. Due to its alkalinity, the tetramethylammonium hydroxide (TMAH) based developer directly transfers the exposed pattern to the hard mask. We subsequently use an oxygen

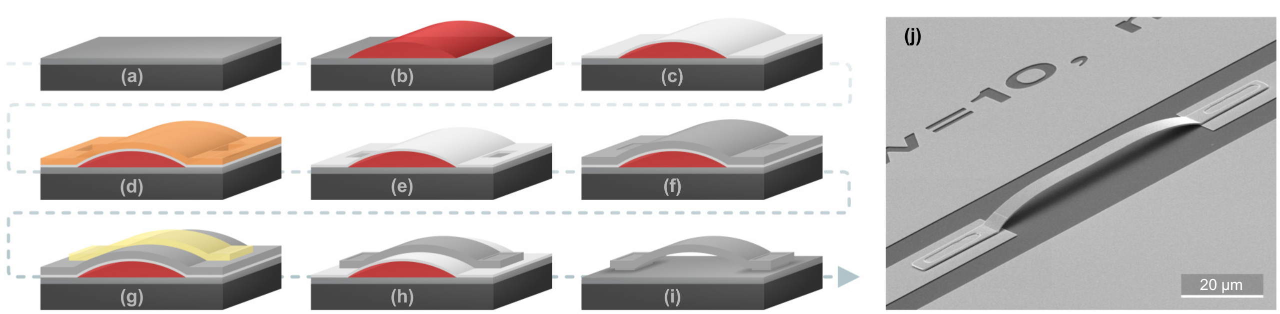

FIG. 1. Fabrication steps of superconducting niobium air bridges: (a) metallization and ground plane patterning with reactive ion etching; (b) optical lithography and reflow of positive resist; (c) angled evaporation of a sacrificial Al hard mask; (d) contact area opening by first defining a thin optical resist mask, followed by wet etching of the hard mask; (e) selective resist removal by oxygen ashing; (f) removal of surface oxides on the Nb groundplane via argon (Ar) ion milling and sputtering of a thick Nb air bridge layer; (g) patterning of optical resist to define lateral bridge dimensions; (h) pattern transfer with SF_6-based reactive ion etching; (i) Al hard mask removal by wet-chemical etching and resist stripping with an N-methyl-2-pyrrolidone-based remover. (j) Scanning electron micrograph of an air bridge with a length of 60 μm and a width of 10 μm.

plasma to selectively remove the top resist without attacking the hard mask and reflowed bottom resist [Fig. 1(e)]. Afterwards, we load the wafer in a sputtering chamber and use argon ion milling to remove surface oxides on the underlying Nb groundplane. This step is essential to ensure galvanic connection between the air bridge and the groundplane. We then sputter-deposit a 900 nm thick layer of Nb. We use a low pressure of 1.3 mTorr to reduce intrinsic stress in the film [33] [Fig. 1(f)]. In our case, optimization of this step has been found to be essential, to ensure high stability of fabricated air bridges. High tensile stress leads to breaking points between the pad and the arch, as further described in Appendix B. Afterwards, we coat the niobium layer with the etch-resistant negative photoresist ma-N 1420 to define the width and length of the air bridge [Fig. 1(g)]. We use an SF_6-based process to etch the top niobium layer in several in situ steps to reduce thermal load and thus prevent reflow of the underlying bottom resist [Fig. 1(h)]. The Al hard mask serves as an etch stopper due to its resilience against SF_6-based etching chemistry. Afterwards, we remove the hard mask with a wet-chemical Al etchant (TechniEtch Al80) at an elevated temperature of 60 °C and use an N-methyl-2-pyrrolidone-based remover to strip the underlying resist [Fig. 1(i)]. The air bridges are dried by nitrogen blow-drying after immersion in hot isopropyl alcohol (IPA), chosen because of its low surface tension coefficient [34]. We avoid using sonication for cleaning, as it might result in rip-offs at the contact areas.

The process, as such, is compatible as an "air-bridge-last" process, i.e., air bridges are fabricated as the last element of a device, since sensitive elements, such as Josephson junctions, are protected by resist during etching. However, by fabricating air bridges before Al-based elements, we are able to employ additional rigorous cleaning steps. We remove potential cross-linked resist and hard mask residues by immersing the chip for 10 min in piranha acid, followed by a 10 min BOE immersion to remove lossy niobium oxides [35]. Afterwards, we immerse the wafer a second time, for 10 min in piranha acid and 20 min in BOE, to remove buried defects and residues in the metal-air interface. A fully processed air bridge is shown in Fig. 1(j). The air bridge has a width of 10 µm and a length of 60 µm. Bridges up to a length of 60 µm show a yield of 100% for approximately 23 500 fabricated air bridges on a 100 mm wafer.

III. AIR BRIDGE CHARACTERIZATION

To ensure galvanic connection and to investigate superconducting properties, we measure resistance as a function of temperature across a daisy chain of six air bridges [cf. Fig. 2(a)]. Each air bridge has a width of 10 µm and a length of 60 µm. The corresponding resistance curve is shown in Fig. 2(b). By fitting two Gaussians to the derivative of the resistance, we identify two superconducting transitions, $T_{c,AB} = 9.32$ K and $T_{c,film} = 9.43$ K. The value for the air bridge transition $T_{c,AB}$ is close to the transition temperature found in the literature [36] and thus indicates that sufficiently high quality Nb films can be grown on Al seed layers. Due to the higher critical temperature of Nb, compared with Al, Nb air bridges can be used in superconducting integrated circuits operating well above 1 K.

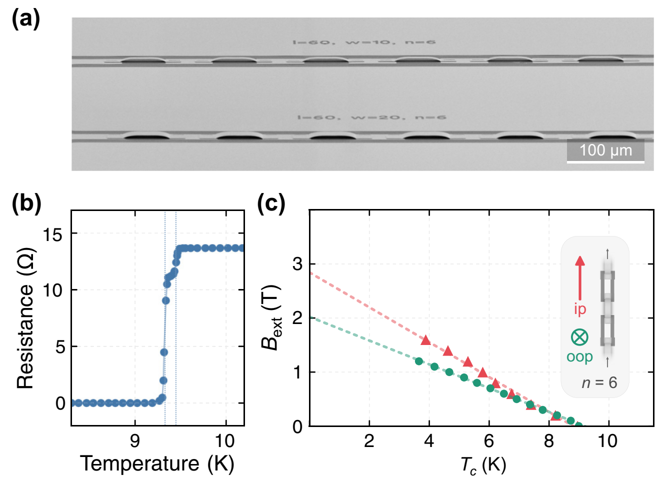

FIG. 2. Transport measurements of several air bridges chained together. (a) Scanning electron micrograph of a daisy chain with $n_{AB} = 6$ air bridges. (b) Resistance vs temperature for the daisy chain at zero magnetic field. The first transition at $T_{c,AB} = 9.32$ K corresponds to the air bridge; the second transition at $T_{c,film} = 9.43$ K corresponds to the thin film ground plane. (c) Magnetic field B_c for in-plane (ip, red) and out-of-plane (oop, green) geometries.

The high T_c also relates to a high upper critical magnetic field $B_{c2,0}$. We extract the critical temperature by applying a constant external magnetic field B_{ext} and sweeping the temperature T. By repeating this measurement for different values of B_{ext}, we can extrapolate the critical field $B_{c2,0}$ at zero temperature by fitting the measured data points to the Ginzburg-Landau theory with $B_{c2}(T) = B_{c2,0}(1 - T/T_c)$. From Fig. 2(c), we extract an upper critical field of $B_{c2,ip} = (2.84 \pm 0.05)$ T for an in-plane (ip) geometry and $B_{c2,oop} = (2.04 \pm 0.02)$ T for an out-of-plane (oop) geometry. Such high critical fields enable the use of air bridges in applications where magnetic fields up to 2 T are needed, such as electron spin resonance spectroscopy [37,38], superconducting qubit experiments [39], or parametric amplifiers that operate at high fields [40].

To analyze the dielectric properties of the air bridges, we probe different CPW resonator configurations and extract the internal quality factor Q_{int} [41]. We measure the complex-valued scattering parameter S_{21} as a function of frequency around the fundamental resonance frequency of each resonator using a vector network analyzer. The data are fitted by a circle fit model, which allows us to extract $Q_{\rm int}$ at different photon numbers [42]. This figure of merit defines the internal loss in our system and can, in particular, be used to extract the additional loss per air bridge [8] by probing resonators with varying numbers of air bridges. The chips are wire-bonded after the chemical treatment and mounted in a dilution refrigerator system operating at a base temperature of 10 mK. We control the number of photons in the CPW resonators by varying the drive power of our signal between −70 dBm and −160 dBm at the sample. The transmitted signal is then amplified by a low-noise high electron mobility transistor (HEMT) and an additional room temperature amplifier. The measurement setup is explained in more detail in Appendix C. We focus on two different resonator configurations: first, the *grounding* configuration, in which we place the air bridge as an additional grounding element across the CPW, and second, the *in-line* configuration, in which we use the air bridge as part of the center conductor of the CPW. Micrographs of the latter device are shown in Figs. 3(a) and 3(b). All resonators are impedance-matched to the 50 Ω microwave environment, with a CPW center conductor width w of 10 µm and a gap g of 6 µm. The $\lambda/4$ resonators are coupled to the feedline with a coupling quality factor of approximately 4×10^6. For both *grounding* air bridges and *in-line* air bridges, we measure a reduction in the internal quality factor on reducing the input power and, therefore, the effective photon number in the resonator [cf. Figures 3(c) and 3(e), respectively]. This is attributed to the TLS loss, as typically observed in superconducting qubits and resonators [43,44].

The *grounding* air bridge chip features 19 resonators with fundamental resonances between 4 and 6 GHz and a number of air bridges $n_{\rm AB}$ varying between 0 and 78. Each grounding air bridge has a width of 20 µm and a length of 60 µm. In the single-photon regime, we reach a mean quality factor of $Q_{\rm int} = (8.23 \pm 1.84) \times 10^6$, with the best-performing resonator, containing 17 grounding air bridges, surpassing $(11.5 \pm 0.4) \times 10^6$. We analyze the internal loss $\delta_{\rm int} \approx \tan\delta_{\rm int} = 1/Q_{\rm int}$ as a function of air bridge number $n_{\rm AB}$ in the high-power (blue) and low-power (orange) regimes. Using a linear regression model with a 95% confidence interval, we fit the data points in the blue shaded region in Fig. 3(d). We exclude the green resonance from the fit, since the extracted internal quality factor has a large uncertainty, owing to a nonlinear response. From the fit, we obtain a negative loss per air bridge in the high-power limit of $(-2.58 \pm 7.11) \times 10^{-11}$, with a resulting coefficient of determination of $R^2 = 0.04$. This clearly shows that the loss per air bridge is below the resolution limit of our resonators. Additionally, we extract the loss per air bridge in the single-photon limit in the orange shaded region in Fig. 3(d). The extracted loss per air bridge of $(4.92 \pm 5.67) \times 10^{-10}$ is an order of magnitude lower, compared with the best reported air bridge fabrication methods [11]. However, as in the high-power regime,

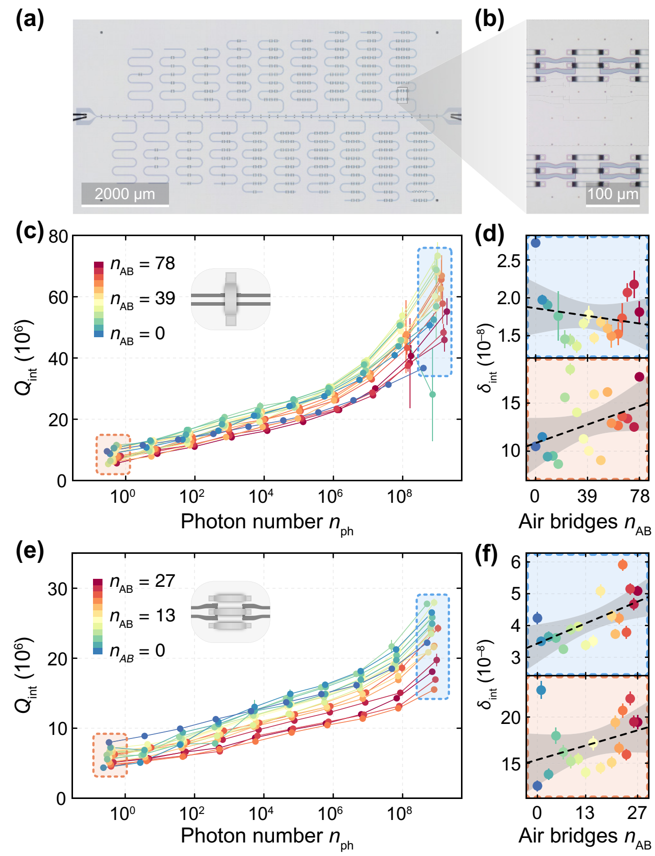

FIG. 3. Coplanar waveguide (CPW) resonator measurements with different air bridge configurations. (a) Optical micrograph of 19 individual $\lambda/4$ resonators coupled to a common feedline. (b) Magnified view of in-line air bridges in the signal line of a CPW. (c) Internal quality factor $Q_{\rm int}$ as a function of photon number for 19 different resonators on a single chip. The number of grounding air bridges is varied between $n_{\rm AB} = 0$ and $n_{\rm AB} = 78$. (d) Internal loss $\delta_{\rm int}$ vs $n_{\rm AB}$ in the high-power (blue) and low-power (orange) regimes for the grounding configuration. As visualized by the gray 95% confidence interval, no clear dependence is visible. (e) Internal quality factor as a function of photon number for 18 different resonators on a single chip. Up to 27 in-line air bridges serve as interconnects of the CPW segments. (f) Loss $\delta_{\rm int}$ vs $n_{\rm AB}$ in the high- and low-power regimes in the in-line configuration. In analogy to (d), no clear dependence on the number of air bridges is visible in the single-photon limit.

the resulting coefficient of determination $R^2 = 0.16$ still indicates that the loss per air bridge is below the resolution limit of the sample. The large uncertainty in the loss estimate arises from the fact that the dissipation per bridge is less than the resonator-to-resonator variation in loss.

We perform an identical analysis for the *in-line* chip with 19 individual resonators that contain between 0 and 27 air bridges. Each in-line air bridge is fabricated with a center conductor width of 10 µm and a length of 60 µm. To imitate CPW crossovers with grounding, each in-line air bridge has two identical passive neighboring air bridges, as shown in Fig. 3(b). One resonance is excluded because of a fabrication defect, probably caused by dust in the coplanar waveguide. The resulting quality factors are visualized as a function of photon number in Fig. 3(e). We obtain a mean quality factor of $Q_{\mathrm{int}} = (6.00 \pm 0.98) \times 10^6$ in the single-photon regime. While the overall quality factor is lower in both the single-photon and high-power regimes, compared with the *grounding* air bridge chip, we attribute this behavior to wafer-to-wafer variations in resonator performance, and not to the air bridge fabrication process itself. This is confirmed by an analysis of the loss per air bridge equivalent to the previous analysis. We extract the loss per air bridge in the high-power regime from the blue shaded region in Fig. 3(f). The obtained loss per air bridge is $(4.89 \pm 3.46) \times 10^{-10}$ with $R^2 = 0.36$. In the single-photon regime (orange), we extract a loss per air bridge of $(1.18 \pm 1.60) \times 10^{-9}$ ($R^2 = 0.13$), which is notably larger, compared with the loss per grounding air bridge. While a larger loss is, in principle, expected, because of a higher participation ratio for in-line air bridges, this increase is mainly attributed to the lower number of air bridges, compared with the grounding resonator sample. By probing 27 instead of 78 bridges, the resolution limit of our resonators is lower, which is reflected in the larger uncertainty.

IV. VACUUM-GAP AIR BRIDGE QUBIT

As the Nb air bridge fabrication process yields stable metallization layers for sizes up to $150 \times 150\,\mu\mathrm{m}^2$, we can utilize air bridges as versatile vacuum-gap capacitors [45]. In particular, we use air bridges as a shunting capacitance of transmon qubits by vertically stacking the capacitor pads. This pushes the energy stored in the electric field from the substrate into loss-free vacuum. Furthermore, because of the larger capacitance per area, the overall footprint of qubits is reduced, similar to designs that utilize flip-chip geometry [46], through-silicon vias [47], or suspended silicon beams [48]. In our design, the bottom capacitor plate has dimensions of $240 \times 60\,\mu\mathrm{m}^2$, and the air bridge on top has a width of $120\,\mu$m and a length of $105\,\mu$m. The height of the bridge is $2.7\,\mu$m. Optical and scanning electron micrographs are shown in Figs. 4(a) and 4(b). We simulate the resulting structure with a finite-element model (FEM) solver to extract the electric field and capacitances. Compared with approximately 10% in conventional coplanar transmons, 42% of the energy stored in the electric field resides in vacuum. Moreover, 86% of the field energy stored in vacuum is located between the capacitor plates.

We fabricate a sample with several air bridge qubits according to the fabrication steps presented in Sec. II. To fabricate the Josephson junction, we use the Manhattan shadow evaporation process [49,50] with a chemically semiamplified resist (CSAR) 6200 bottom resist and a polymethyl methacrylate (PMMA) 950k top resist mask.

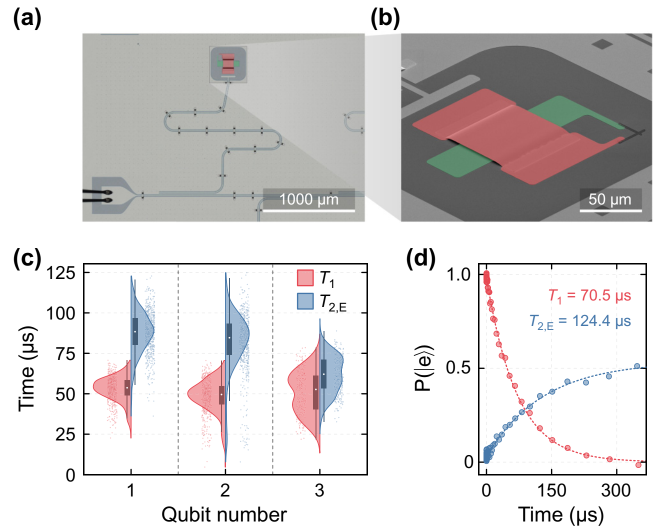

FIG. 4. Transmon qubit with vacuum-gap capacitance. (a) Optical micrograph of vacuum-gap air bridge qubit. The bottom island is highlighted in green, the top island, including the bridge, in red. (b) Scanning electron micrograph of fabricated air bridge qubit. The Josephson junction is highlighted in black. (c) Time domain measurements of three air bridge qubits, averaged over 100 h. The left side of the violin plot (red) visualizes the histogram of the lifetime T_1, whereas the right side (blue) visualizes the echo coherence time $T_{2,\mathrm{E}}$. Individual traces are visualized as single points in the corresponding color. (d) Single trace of a qubit lifetime T_1 and coherence time $T_{2,\mathrm{E}}$ from qubit 2.

The bottom and top Al electrodes have thicknesses of 30 and 70 nm, respectively. After junction fabrication, we galvanically connect the Al to the Nb groundplane using an ex situ Al bandaging process [51]. The junction fabrication process is explained in more detail in Appendix A. The air bridge qubits have transition frequencies between 4.3 and 5.3 GHz and a charging energy E_{C} between 240 and 245 MHz. They are dispersively coupled to readout resonators with fundamental frequencies between 6.9 and 7.4 GHz and a coupling strength of 60 MHz between resonator and qubit. To acquire statistically relevant data, we measure three air bridge qubits on one sample over 100 h in two cooldowns. The resulting data are visualized in Fig. 4(c) as a violin plot. The median lifetimes T_1 (red) for all three qubits are in the range of 49.4 to $53.5\,\mu$s, with single traces exceeding $75\,\mu$s. Example single traces are shown in Fig. 4(d). Median echo coherence times $T_{2,\mathrm{E}}$ (blue) are 88.3 and $84.3\,\mu$s for qubits 1 and 2, respectively. The coherence time $T_{2,\mathrm{E}} = 62\,\mu$s of qubit 3 is lower, since it has been measured in a dilution refrigerator setup with less filters. The median T_1 time is reduced by a factor of 2–5, compared with state-of-the-art coplanar Nb transmons [52,53]. We attribute this to the higher metal-air interface participation ratio in the vacuum-gap air bridge qubit, since amorphous Nb oxides are known to be a major loss channel in transmon qubits [52].

V. CONCLUSION AND OUTLOOK

In conclusion, we have demonstrated an air bridge fabrication process based on a patterned hard mask, which is highly scalable and enables high yield, owing to its subtractive processing approach. By incorporating several cleaning steps, we show that the extracted single-photon losses, per grounding air bridge of $\delta_{\mathrm{AB}} = (4.92 \pm 5.67) \times 10^{-10}$ and per in-line air bridge of $\delta_{\mathrm{AB}} = (1.18 \pm 1.60) \times 10^{-9}$, remain below the resolution limit of the resonator-based measurement. Furthermore, we have verified that the fabricated air bridges support superconductivity up to 9.3 K at zero magnetic field and up to 3.9 K in a magnetic field of 1.6 T. This extends their applicability to high magnetic fields and temperatures above 4 K, which is not feasible with conventional aluminum-based approaches.

An open question that has not been addressed is the long-term stability, as Nb resonators are known to oxidize and decrease in quality over time [54]. While we wanted to focus on the process itself within this study, we are planning on investigating the aging behavior, as well as the compatibility with surface treatments, such as buffer and capping materials, to avoid aging [52].

Beyond their use as interconnects, air bridges can also serve as active elements in tunable coupler qubits [11,55]. The demonstrated low-loss air bridges hold significant potential for reducing coupler-induced decoherence, compared with existing fabrication techniques. Additionally, we have shown that large air bridges can function as capacitors in transmon qubits, yielding a median qubit lifetime of $T_1 = 51.6\,\mu\mathrm{s}$. While the dominant decoherence mechanisms require further investigation, this qubit design offers the potential for a smaller footprint, compared with planar transmons, by reducing the bridge height and increasing capacitance. Moreover, the confinement of the electric field between capacitor leads enhances robustness against misalignment in three-dimensional (3D) integrated qubit architectures.

Finally, since the resist is protected by the hard mask during milling and deposition, our process is compatible with a variety of other materials, including Ta and NbTiN, as well as any material that remains intact during the hard mask removal process. This versatility makes the proposed fabrication technique well-suited for a wide range of micro- and nanoelectronic devices, not only superconducting circuits.

ACKNOWLEDGMENTS

This work received financial support from the German Federal Ministry of Education and Research via the funding program “Quantum technologies—from basic research to the market” under Contracts No. 13N15680 (GeQCoS) and No. 13N16188 (MUNIQC-SC), from the Deutsche Forschungsgemeinschaft (DFG, German Research Foundation) via Project No. FI2549/1-1 and via the Germany’s Excellence Strategy EXC- 2111-390814868 “MCQST,” as well as from the European Union via the EU Flagship on Quantum Technology HORIZON-CL4-2022-QUANTUM-01-SGA Project 101113946 OpenSuperQ-Plus100. The research is part of the Munich Quantum Valley, which is supported by the Bavarian state government with funds from the Hightech Agenda Bayern Plus.

N.B. and L.K. contributed equally to this work.

DATA AVAILABILITY

The data that support the findings of this article are openly available [56].

APPENDIX A: QUBIT FABRICATION

To fabricate Josephson junctions, we use the well-established Manhattan shadow evaporation process. However, to realize Josephson junction sizes of the order of $100 \times 100\,\mathrm{nm}^2$, the total electron beam lithography (EBL) resist height does not exceed $1\,\mu\mathrm{m}$ for sufficiently large aspect ratios. The air bridge is thus higher than the resist and needs to be protected with an additional optical lithography step to prevent lift-off tear-offs of Al at the air bridge interface.

The fabrication steps are visualized in Fig. 5. We start the Josephson junction fabrication process by spin coating a 650 nm thick bottom layer of CSAR 6200, followed by a less sensitive 350 nm thick top layer of PMMA 950 K. To exploit complementary exposure techniques and developers, we coat the top layer with an additional 50 nm of CSAR 6200. As a last step, we coat the chip with a thick layer of optically sensitive resist mr-DWL 5, which is selectively removed around air bridges in a solvent-based developer (mr-Dev 600). The thin sacrificial CSAR layer serves to protect the underlying PMMA from being attacked by the optical developer. Afterwards, we expose and develop the EBL resist and evaporate Al at a tilt of 35° with rotations of 0° and 90° to fabricate Josephson junctions. During deposition, the air bridges are fully protected by the resist, which prevents Al tear-offs in the lift-off process step.

In a subsequent step we repeat this process to fabricate ex situ bandages with an additional milling step prior to Al deposition.

APPENDIX B: NIOBIUM FILM STRESS

To ensure a high yield of air bridges, it was essential for us to optimize the Nb sputtering conditions. Our typical sputtering regime utilizes an argon partial pressure of 3.3 mTorr. However, the air bridge metallization layer bends due to the high intrinsic stress that results from the sputtering conditions [57]. This is clearly visible in the center part of the 300 nm thick air bridge in Fig. 6(a). In

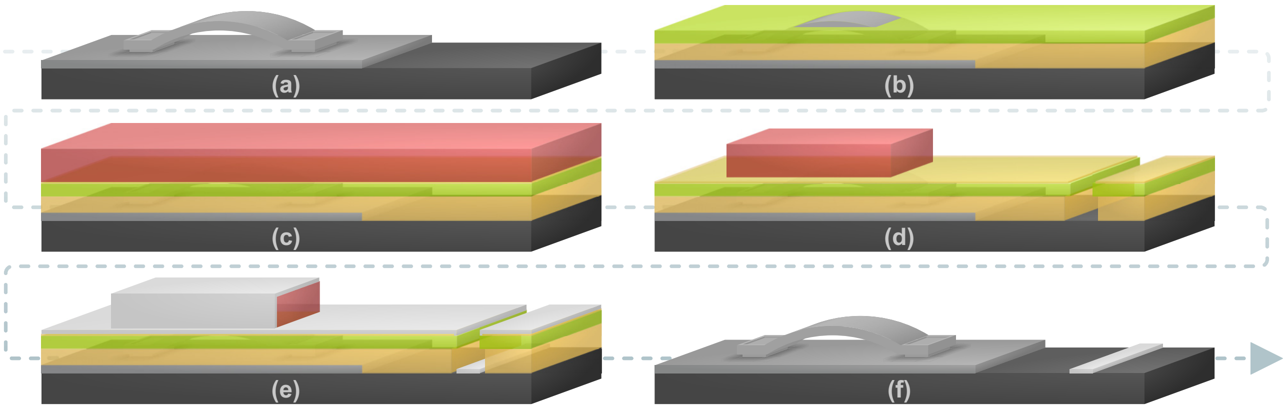

FIG. 5. Fabrication steps to protect air bridges during Josephson junction fabrication, not to scale. (a) Chip with patterned groundplane and finished air bridges. (b) Spin coating of bilayer electron beam lithography resist. (c) Coating of additional bilayer consisting of a sacrificial chemically semiamplified resist layer and a thick optical resist. (d) Subsequent exposure and development of optical resist and electron beam resist. (e) Double angle shadow evaporation of Al to form Josephson junctions. (f) Tear-off-free lift-off.

particular, this can lead to breaking points and ultimately to collapses [Fig. 6(c)]. At an even higher partial pressure, the film peels off after deposition. By reducing the partial pressure, we were able to reduce tensile stress in our film. An example of a relaxed air bridge sputtered at a lower pressure of 2.0 mTorr is shown in Fig. 6(b). We hope to quantify the intrinsic stress and further optimize the yield for higher bridge lengths by employing local asymmetric and Bragg-Brentano x-ray diffraction configurations [58].

APPENDIX C: MEASUREMENT SETUP

The sample is mounted at the mixing chamber stage of a dilution refrigerator (Bluefors Fast Sample Exchange cryostat or Qinu Sionludi L). Figure 7 shows the electronic wiring from room temperature up to several millikelvins. We use two different devices for measurements: resonators are probed with a Keysight vector network analyzer (VNA); qubits are controlled and read out with a Zurich Instruments quantum controller (SHFQC). We attenuate the input signal by a total of 81 dB. In addition, we characterized the cable loss in the input line, which resulted in an additional 8 dB of loss at 4 GHz. We take this into account for all frequencies when determining the estimated photon number in the $\lambda/4$ resonators. For measurements in the Bluefors cryostat, the output signal is routed through a switch, the Qinu cryostat does not contain a switch. Two dual-junction isolators ensure unidirectional signal routing. An additional high-pass filter (Minicircuits VHF-3100+) protects the sample from noise. We amplify the transmitted signal with a HEMT amplifier at the 4-K stage of the cryostat, and an additional low-noise amplifier (LNA) at room temperature. The sample is wire-bonded to a gold-coated printed circuit board (PCB) and placed inside a copper package. The package is located inside two cryoperm shields to protect the sample from stray magnetic fields. An example resonator response at 5.1 GHz with 31 grounding air bridges is shown in Fig. 8. The red trace is measured at a drive power of -70 dBm, corresponding to roughly 10^9 photons. The blue trace is measured at

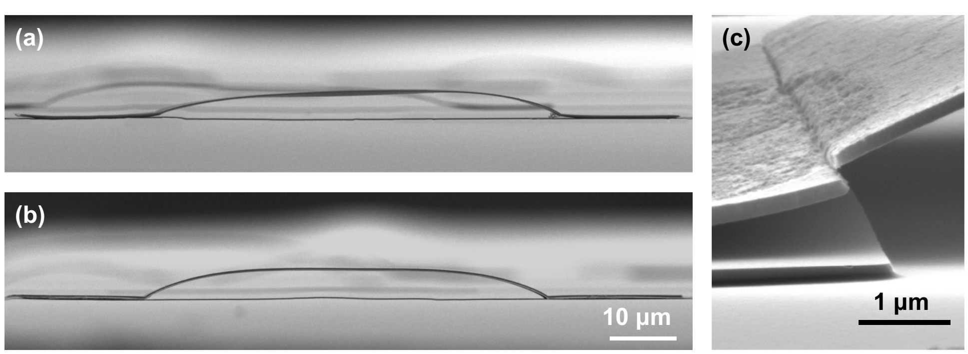

FIG. 6. Scanning electron micrograph of air bridges sputtered at different process conditions. (a) Air bridge sputtered at a partial pressure of 3.3 mTorr. The center is bent due to tensile stress in the film. (b) Air bridge sputtered at a partial pressure of 2.0 mTorr. (c) Broken connection between bridge and pad for a tensile stressed air bridge.

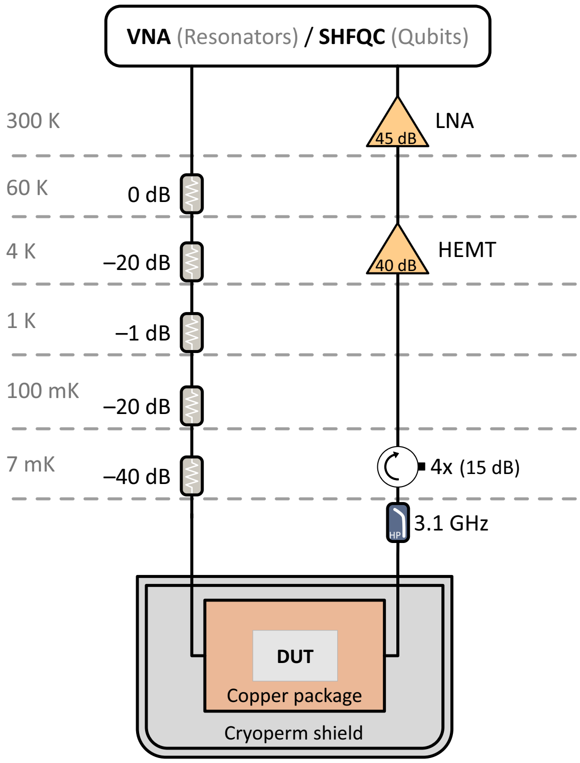

FIG. 7. Measurement setup for both resonator and qubit devices. DUT, device under test; HEMT, high electron mobility transistor; LNA, low-noise amplifier; VNA, vector network analyzer. For details, see main text.

a drive power of −160 dBm, which resembles roughly 1 photon. The single-photon quality factor of this trace corresponds to $Q_{\text{int}} = (11.05 \pm 0.28) \times 10^6$. For a drive power of −70 dBm, we fit an internal quality factor of $Q_{\text{int}} = (59.5 \pm 2.6) \times 10^6$. Although the signal-to-noise-ratio is significantly better, the uncertainty in Q_{int} is larger, owing to undercoupling, arising from the constant coupling quality factor of $Q_c = 4.1 \times 10^6$. We try to achieve critical

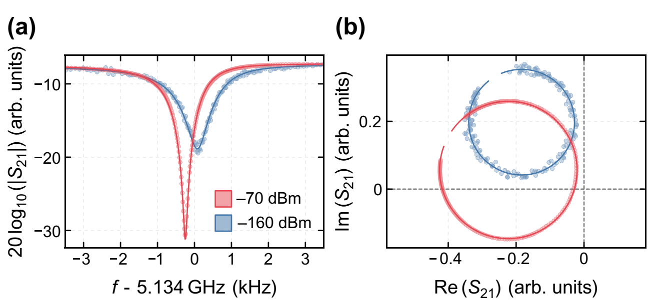

FIG. 8. Example measurement trace of a resonator containing 31 grounding air bridges. (a) Magnitude of S_{21} plotted against the frequency for both single photons (blue) and 10^9 photons (red). Circles correspond to measurement points; the solid line corresponds to the fit. (b) The same traces, plotted in the complex plane.

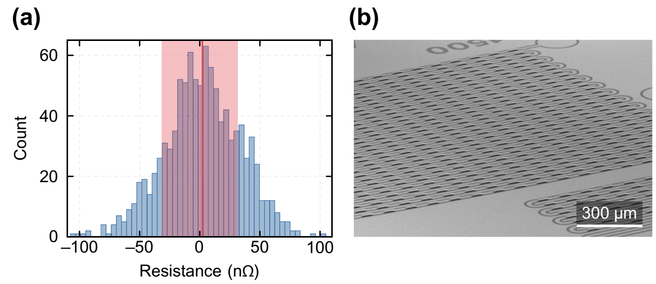

FIG. 9. DC conductivity measurements of 1500 air bridges in series at 3 K to extract the resistance of the metal-metal interface between groundplane and air bridge. (a) Histogram of 1000 measurement shots, resulting in a mean total resistance R_{tot} of 2 nΩ and a standard deviation σ of 32 nΩ. (b) Scanning electron micrograph of measured device with chain of 1500 air bridges.

coupling of our resonators in the low-power regime, as this is the main region of interest. Also, the strong drive power starts to result in a slight nonlinearity, which we attribute to the saturation limit of our HEMT amplifier.

APPENDIX D: DC CONDUCTIVITY

To investigate the resistivity of the metal-metal interface between ground plane and air bridge, we fabricated a daisy chain consisting of 1500 air bridges in series, each with a pad size of $15 \times 15\,\mu\text{m}^2$, resulting in a total interface area of $1500 \times 2 \times 15\,\mu\text{m} \times 15\,\mu\text{m} = 0.675\,\text{mm}^2$. The histogram of 1000 measurement shots measured at 3 K with a current of 100 mA is shown in Fig. 9. We measure a resistance of $R_{\text{tot}} = 2 \pm 32\,\text{n}\Omega$ at 3 K, corresponding to a contact resistance of $R = (3 \pm 47)\,\text{f}\Omega/\mu\text{m}^2$. This confirms a low-ohmic galvanic connection between ground plane and air bridge.

[1] S. Krinner, N. Lacroix, A. Remm, A. Di Paolo, E. Genois, C. Leroux, C. Hellings, S. Lazar, F. Swiadek, J. Herrmann, G. J. Norris, C. K. Andersen, M. Müller, A. Blais, C. Eichler, and A. Wallraff, Realizing repeated quantum error correction in a distance-three surface code, Nature **605**, 669 (2022).

[2] S. Vallés-Sanclemente, S. L. M. Van Der Meer, M. Finkel, N. Muthusubramanian, M. Beekman, H. Ali, J. F. Marques, C. Zachariadis, H. M. Veen, T. Stavenga, N. Haider, and L. DiCarlo, Post-fabrication frequency trimming of coplanar-waveguide resonators in circuit QED quantum processors, Appl. Phys. Lett. **123**, 034004 (2023).

[3] R. N. Simons, *Coplanar Waveguide Circuits, Components, and Systems*, edited by K. Chang, Wiley Series in Microwave and Optical Engineering (John Wiley & Sons, Inc., New York, USA, 2001).

[4] G. Ponchak, J. Papapolymerou, and M. Tentzeris, Excitation of coupled slotline mode in finite-ground CPW with unequal ground-plane widths, IEEE Trans. Microw. Theory Tech. **53**, 713 (2005).

[5] F. Arute *et al.*, Quantum supremacy using a programmable superconducting processor, Nature **574**, 505 (2019).

[6] S. Cao *et al.*, Generation of genuine entanglement up to 51 superconducting qubits, Nature **619**, 738 (2023).

[7] M. Schicke and K. Schuster, Integrated niobium thin film air bridges as variable capacitors for superconducting GHz electronic circuits, IEEE Trans. Appl. Supercond. **13**, 135 (2003).

[8] Z. Chen, A. Megrant, J. Kelly, R. Barends, J. Bochmann, Y. Chen, B. Chiaro, A. Dunsworth, E. Jeffrey, J. Y. Mutus, P. J. J. O'Malley, C. Neill, P. Roushan, D. Sank, A. Vainsencher, J. Wenner, T. C. White, A. N. Cleland, and J. M. Martinis, Fabrication and characterization of aluminum airbridges for superconducting microwave circuits, Appl. Phys. Lett. **104**, 052602 (2014).

[9] A. Dunsworth *et al.*, A method for building low loss multi-layer wiring for superconducting microwave devices, Appl. Phys. Lett. **112**, 063502 (2018).

[10] Y. Sun, J. Ding, X. Xia, X. Wang, J. Xu, S. Song, D. Lan, J. Zhao, and Y. Yu, Fabrication of airbridges with gradient exposure, Appl. Phys. Lett. **121**, 074001 (2022).

[11] K. Bu, S. Huai, Z. Zhang, D. Li, Y. Li, J. Hu, X. Yang, M. Dai, T. Cai, Y.-C. Zheng, and S. Zhang, Tantalum air-bridges for scalable superconducting quantum processors, npj Quantum Inf. **11**, 17 (2025).

[12] L. D. Alegria, A. Abelson, E. Kim, S. Im, P. M. Voyles, V. Lordi, J. L. DuBois, and Y. J. Rosen, Growth and structure of alpha-Ta films for quantum circuit integration, J. Appl. Phys. **137**, 044402 (2025).

[13] E. Girgis, J. Liu, and M. L. Benkhedar, Fabrication of metallic air bridges using multiple-dose electron beam lithography, Appl. Phys. Lett. **88**, 202103 (2006).

[14] A. Khalid, C. Li, J. Grant, S. Saha, S. Ferguson, and D. R. Cumming, Simple e-beam air-bridge technology for mm-wave applications, Microelectron. Eng. **98**, 262 (2012).

[15] Y. Jin, M. Moreno, P. M. T. Vianez, W. K. Tan, J. P. Griffiths, I. Farrer, D. A. Ritchie, and C. J. B. Ford, Microscopic metallic air-bridge arrays for connecting quantum devices, Appl. Phys. Lett. **118**, 162108 (2021).

[16] N. Janzen, M. Kononenko, S. Ren, and A. Lupascu, Aluminum air bridges for superconducting quantum devices realized using a single-step electron-beam lithography process, Appl. Phys. Lett. **121**, 094001 (2022).

[17] T. Stavenga, S. A. Khan, Y. Liu, P. Krogstrup, and L. DiCarlo, Lower-temperature fabrication of airbridges by grayscale lithography to increase yield of nanowire transmons in circuit QED quantum processors, Appl. Phys. Lett. **123**, 024004 (2023).

[18] H.-R. Tao, C. Zhang, L. Du, X.-X. Yang, L.-L. Guo, Y. Chen, H.-F. Zhang, Z.-L. Jia, W.-C. Kong, P. Duan, and G.-P. Guo, Fabrication and characterization of low loss niobium airbridges for superconducting quantum circuits, Appl. Phys. Lett. **125**, 034001 (2024).

[19] Y. Wu *et al.*, Strong quantum computational advantage using a superconducting quantum processor, Phys. Rev. Lett. **127**, 180501 (2021).

[20] N. D. Korshakov, D. O. Moskalev, A. A. Soloveva, D. A. Moskaleva, E. S. Lotkov, A. R. Ibragimov, M. V. Androschuk, I. A. Ryzhikov, Y. V. Panfilov, and I. A. Rodionov, Aluminum Josephson junction microstructure and electrical properties modified by thermal annealing, Sci. Rep. **14**, 26066 (2024).

[21] J. B. Hertzberg, E. J. Zhang, S. Rosenblatt, E. Magesan, J. A. Smolin, J.-B. Yau, V. P. Adiga, M. Sandberg, M. Brink, J. M. Chow, and J. S. Orcutt, Laser-annealing Josephson junctions for yielding scaled-up superconducting quantum processors, npj Quantum Inf. **7**, 129 (2021).

[22] E. J. Zhang *et al.*, High-performance superconducting quantum processors via laser annealing of transmon qubits, Sci. Adv. **8**, eabi6690 (2022).

[23] D. K. Finnemore, T. F. Stromberg, and C. A. Swenson, Superconducting properties of high-purity niobium, Phys. Rev. **149**, 231 (1966).

[24] S. Krinner, S. Storz, P. Kurpiers, P. Magnard, J. Heinsoo, R. Keller, J. Lütolf, C. Eichler, and A. Wallraff, Engineering cryogenic setups for 100-qubit scale superconducting circuit systems, EPJ Quantum Technol. **6**, 2 (2019).

[25] A. Anferov, A. Suleymanzade, A. Oriani, J. Simon, and D. I. Schuster, Millimeter-wave four-wave mixing via kinetic inductance for quantum devices, Phys. Rev. Appl. **13**, 024056 (2020).

[26] A. Anferov, K.-H. Lee, F. Zhao, J. Simon, and D. I. Schuster, Improved coherence in optically defined niobium trilayer-junction qubits, Phys. Rev. Appl. **21**, 024047 (2024).

[27] A. Chandrasekaran, R. W. Van De Kruijs, J. M. Sturm, and F. Bijkerk, Nb texture evolution and interdiffusion in Nb/Si-layered systems, ACS Appl. Mater. Interfaces **13**, 31260 (2021).

[28] A. A. Murthy, P. Masih Das, S. M. Ribet, C. Kopas, J. Lee, M. J. Reagor, L. Zhou, M. J. Kramer, M. C. Hersam, M. Checchin, A. Grassellino, R. dos Reis, V. P. Dravid, and A. Romanenko, Developing a chemical and structural understanding of the surface oxide in a niobium superconducting qubit, ACS Nano **16**, 17257 (2022).

[29] C. M. Quintana *et al.*, Characterization and reduction of microfabrication-induced decoherence in superconducting quantum circuits, Appl. Phys. Lett. **105**, 062601 (2014).

[30] Y. Okuyama, T. Hashimoto, and T. Koguchi, High dose ion implantation into photoresist, J. Electrochem. Soc. **125**, 1293 (1978).

[31] J. Tian and M. Bartek, in *2008 58th Electronic Components and Technology Conference* (IEEE, Piscataway, NJ, USA, 2008), pp. 1787–1792.

[32] D. S. Wisbey, J. Gao, M. R. Vissers, F. C. S. da Silva, J. S. Kline, L. Vale, and D. P. Pappas, Effect of metal/substrate interfaces on radio-frequency loss in superconducting coplanar waveguides, J. Appl. Phys. **108**, 093918 (2010).

[33] T. Imamura, S. Ohara, and S. Hasuo, Bias-sputtered Nb for reliable wirings in Josephson circuits, IEEE Trans. Magn. **27**, 3176 (1991).

[34] A. N. Bolgar, D. A. Kalacheva, V. B. Lubsanov, A. Y. Dmitriev, E. S. Alekseeva, E. V. Korostylev, and O. V. Astafiev, Highly stable aluminum air-bridges with stiffeners, J. Appl. Phys. **137**, 154401 (2025).

[35] M. V. P. Altoé, A. Banerjee, C. Berk, A. Hajr, A. Schwartzberg, C. Song, M. Alghadeer, S. Aloni, M. J. Elowson, J. M. Kreikebaum, E. K. Wong, S. M. Griffin, S. Rao, A. Weber-Bargioni, A. M. Minor, D. I. Santiago,

S. Cabrini, I. Siddiqi, and D. F. Ogletree, Localization and mitigation of loss in niobium superconducting circuits, PRX Quantum **3**, 020312 (2022).
[36] J. Rairden and C. Neugebauer, Critical temperature of niobium and tantalum films, Proc. IEEE **52**, 1234 (1964).
[37] A. Bienfait, J. J. Pla, Y. Kubo, M. Stern, X. Zhou, C. C. Lo, C. D. Weis, T. Schenkel, M. L. W. Thewalt, D. Vion, D. Esteve, B. Julsgaard, K. Mølmer, J. J. L. Morton, and P. Bertet, Reaching the quantum limit of sensitivity in electron spin resonance, Nat. Nanotechnol. **11**, 253 (2016).
[38] Z. Wang, L. Balembois, M. Rančić, E. Billaud, M. Le Dantec, A. Ferrier, P. Goldner, S. Bertaina, T. Chanelière, D. Esteve, D. Vion, P. Bertet, and E. Flurin, Single-electron spin resonance detection by microwave photon counting, Nature **619**, 276 (2023).
[39] J. Krause, C. Dickel, E. Vaal, M. Vielmetter, J. Feng, R. Bounds, G. Catelani, J. M. Fink, and Y. Ando, Magnetic field resilience of three-dimensional transmons with thin-film $Al/AlO_x/Al$ Josephson junctions approaching 1 T, Phys. Rev. Appl. **17**, 034032 (2022).
[40] L. Janssen, G. Butseraen, J. Krause, A. Coissard, L. Planat, N. Roch, G. Catelani, Y. Ando, and C. Dickel, Magnetic field dependence of a Josephson traveling-wave parametric amplifier and integration into a high-field setup, Phys. Rev. Appl. **22**, 054018 (2024).
[41] C. R. H. McRae, H. Wang, J. Gao, M. R. Vissers, T. Brecht, A. Dunsworth, D. P. Pappas, and J. Mutus, Materials loss measurements using superconducting microwave resonators, Rev. Sci. Instrum. **91**, 091101 (2020).
[42] S. Probst, F. B. Song, P. A. Bushev, A. V. Ustinov, and M. Weides, Efficient and robust analysis of complex scattering data under noise in microwave resonators, Rev. Sci. Instrum. **86**, 024706 (2015).
[43] W. A. Phillips, Two-level states in glasses, Rep. Prog. Phys. **50**, 1657 (1987).
[44] C. Müller, J. H. Cole, and J. Lisenfeld, Towards understanding two-level-systems in amorphous solids: Insights from quantum circuits, Rep. Prog. Phys. **82**, 124501 (2019).
[45] K. Cicak, D. Li, J. A. Strong, M. S. Allman, F. Altomare, A. J. Sirois, J. D. Whittaker, J. D. Teufel, and R. W. Simmonds, Low-loss superconducting resonant circuits using vacuum-gap-based microwave components, Appl. Phys. Lett. **96**, 093502 (2010).
[46] X. Li *et al.*, Vacuum-gap transmon qubits realized using flip-chip technology, Appl. Phys. Lett. **119**, 184003 (2021).
[47] T. M. Hazard, W. Woods, D. Rosenberg, R. Das, C. F. Hirjibehedin, D. K. Kim, J. M. Knecht, J. Mallek, A. Melville, B. M. Niedzielski, K. Serniak, K. M. Sliwa, D. R. W. Yost, J. L. Yoder, W. D. Oliver, and M. E. Schwartz, Characterization of superconducting through-silicon vias as capacitive elements in quantum circuits, Appl. Phys. Lett. **123**, 154004 (2023).
[48] M. Zemlicka, E. Redchenko, M. Peruzzo, F. Hassani, A. Trioni, S. Barzanjeh, and J. Fink, Compact vacuum-gap transmon qubits: Selective and sensitive probes for superconductor surface losses, Phys. Rev. Appl. **20**, 044054 (2023).
[49] M. V. Costache, G. Bridoux, I. Neumann, and S. O. Valenzuela, Lateral metallic devices made by a multiangle shadow evaporation technique, J. Vac. Sci. Technol. B, Nanotechnol. Microelectron.: Mater., Process., Meas., Phenom. **30**, 04E105 (2012).
[50] J. M. Kreikebaum, K. P. O'Brien, A. Morvan, and I. Siddiqi, Improving wafer-scale Josephson junction resistance variation in superconducting quantum coherent circuits, Supercond. Sci. Technol. **33**, 06LT02 (2020).
[51] A. Dunsworth *et al.*, Characterization and reduction of capacitive loss induced by sub-micron Josephson junction fabrication in superconducting qubits, Appl. Phys. Lett. **111**, 022601 (2017).
[52] M. Bal *et al.*, Systematic improvements in transmon qubit coherence enabled by niobium surface encapsulation, npj Quantum Inf. **10**, 43 (2024).
[53] M. Tuokkola, Y. Sunada, H. Kivijärvi, J. Albanese, L. Grönberg, J.-P. Kaikkonen, V. Vesterinen, J. Govenius, and M. Möttönen, Methods to achieve near-millisecond energy relaxation and dephasing times for a superconducting transmon qubit, Nat. Commun. 16, 5421 (2025).
[54] J. Verjauw, A. Potočnik, M. Mongillo, R. Acharya, F. Mohiyaddin, G. Simion, A. Pacco, T. Ivanov, D. Wan, A. Vanleenhove, L. Souriau, J. Jussot, A. Thiam, J. Swerts, X. Piao, S. Couet, M. Heyns, B. Govoreanu, and I. Radu, Investigation of microwave loss induced by oxide regrowth in high-Q niobium resonators, Phys. Rev. Appl. **16**, 014018 (2021).
[55] C. W. Warren, J. Fernández-Pendás, S. Ahmed, T. Abad, A. Bengtsson, J. Biznárová, K. Debnath, X. Gu, C. Križan, A. Osman, A. Fadavi Roudsari, P. Delsing, G. Johansson, A. Frisk Kockum, G. Tancredi, and J. Bylander, Extensive characterization and implementation of a family of three-qubit gates at the coherence limit, npj Quantum Inf. **9**, 44 (2023).
[56] N. Bruckmoser, L. Koch, I. Tsitsilin, M. Grammer, S. Lasse, and S. Filipp, Supporting data for "Niobium air bridges as low-loss components for superconducting quantum hardware", Zenodo, 2025, https://doi.org/10.5281/zenodo.17920650.
[57] T. Imamura and S. Hasuo, Effects of intrinsic stress on submicrometer Nb/AlO/sub x//Nb Josephson junctions, IEEE Trans. Magn. **25**, 1119 (1989).
[58] F. Motazedian, Z. Wu, J. Zhang, B. Samsam Shariat, D. Jiang, M. Martyniuk, Y. Liu, and H. Yang, Determining intrinsic stress and strain state of fibre-textured thin films by X-ray diffraction measurements using combined asymmetrical and Bragg-Brentano configurations, Mater. Des. **181**, 108063 (2019).